Computational Simulation of Emission Spectra from Shock-Layer Flows in an Arcjet Facility

Tahir Gökçen,* Chung S. Park,† Mark E. Newfield,‡ and Douglas G. Fletcher‡

NASA Ames Research Center, Moffett Field, California 94035

This paper reports computational comparisons with experimental studies of a nonequilibrium blunt-body shock-layer flow in a high-enthalpy arcjet wind tunnel at NASA Ames Research Center. The experimental data include spatially resolved emission spectra of radiation emanating from a shock layer formed in front of a flat-faced cylinder model. Multitemperature nonequilibrium codes are used to compute the conical nozzle flow, supersonic jet, and shock-layer flow. A line-of-sight (LOS) radiation code is employed to predict the spectra from the computed flowfield. Computed LOS emission intensities are directly compared with the experimental data at several axial locations along the stagnation streamline. Various LOS-averaged flow properties, such as vibrational and rotational temperatures, and species number densities, deduced from the experimental spectra, are compared with computed results. Comparisons provide an assessment of thermochemical equilibration processes in an arcjet shock layer.

Introduction

THE flows in arcjet facilities are extremely complex because of several nonequilibrium processes occurring at various portions of the facility. The ability to predict the flow properties realistically in these facilities requires that our current models and codes be advanced and validated against the experimental data. Most of the existing codes have been developed to simulate the equilibrium or nonequilibrium flow in the shock layer forming ahead of a blunt body at hypersonic flight. However, the characteristics of the flow over a blunt body in an arcjet facility are quite different from those in free flight. The flow in an arcjet is produced by passing air, usually mixed with argon, through an electric arc discharge, where energy is added to the flow. The test gas is then expanded through a high-expansion-ratio supersonic nozzle into an evacuated test chamber to produce high velocities. The nonequilibrium expansion process freezes the flow composition near the nozzle throat, where the flow remains vibrationally excited and dissociated. Characterization of the arcjet test flow is a difficult task, partly because of difficulties in obtaining detailed flow measurements. Reviews of the existing experimental data and arcjet characterization work can be found in Refs. 1–3.

Over the years, several experiments have been conducted at NASA Ames arcjet facilities to characterize the arcjet test flow.[2,3] Recently, as part of ongoing arcjet characterization work, spectroscopic radiation emission experiments have been conducted at the 20-MW NASA Ames Research Center's arcjet facility. The emission spectra were obtained from the arcjet freestream and from a shock layer formed in front of flat-faced models.[4] Analysis of the data is expected to provide valuable information about the thermodynamic state of the gas in the arcjet freestream and shock layer as well as details of thermochemical equilibration processes behind the shock wave. Knowledge of the thermodynamic state of the gas in

arcjet test flows and particularly within the shock layer is essential to interpret the heat transfer measurements, such as in surface catalysis experiments. Also, if there were a thermochemical equilibrium region within the shock layer, emission measurements (or temperature) along with the surface pressure measurement would be sufficient to determine the total flow enthalpy.

Objectives of the present work are to present computational simulations of the emission experiments conducted at NASA Ames Research Center's arcjet facility[4] and to investigate the existence of a thermochemical equilibrium region within the shock layer. In these experiments, the pressure behind the shock wave is relatively high so that the shock-layer flow is more likely to have a thermochemical equilibrium region. The existence of such an equilibrium region is of interest for the following reasons: 1) to understand the equilibration processes behind the shock in an arcjet flow environment, 2) to interpret surface heat transfer measurements in arcjets, and 3) to determine the total enthalpy from the spectroscopic measurements.

Facility and Experimental Data

Experimental data were obtained in the NASA Ames Research Center's 20-MW Aerodynamic Heating Facility (AHF). Figure 1 depicts sketches of the facility and line-of-sight (LOS) radiation measurements. This facility, operating with a set of conical nozzles, uses a constricted arc heater to provide high-enthalpy-dissociated nitrogen or airflows for materials testing.[5] Because constricted arc heaters generally produce high enthalpy levels at relatively low pressures, the present experiments were conducted with the AHF 12-in. nozzle configuration to achieve a relatively high surface pressure, and with a 6-in.-diam. flat-faced model to produce a relatively large shock standoff distance for thermochemical equilibration. The AHF 12-in. conical nozzle has a constant area throat with a diameter of 3.81 cm (1.5 in.), converging section with an entrance diameter of 7.65 cm (3.013 in.), and diverging section with an exit diameter of 30.48 cm (12 in.). The conical converging and diverging sections have half-angles of 45 and 8 deg, respectively. The nozzle is connected to the transition section of the arcjet with another converging conical duct with a half-angle of 22 deg.

The experimental data include emission spectra of radiation emanating from a shock layer formed in front of a 6-in.-diam flat-faced cylinder model. The measurements, obtained using a two-dimensional charge-coupled device (CCD) camera

*Senior Research Scientist, Thermosciences Institute. Member AIAA.

†Research Scientist, Thermosciences Institute. Member AIAA.

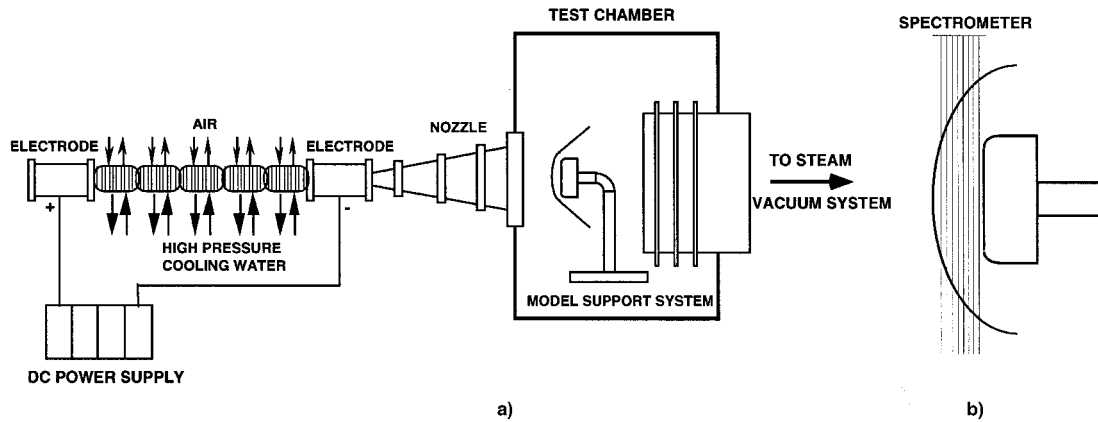‡Research Scientist, Reacting Flow Environments Branch. Member AIAA.

Fig. 1   Sketches of a) NASA Ames Research Center's 20-MW arcjet facility and b) LOS radiation measurements.

mounted on a spectrograph, provide spatially resolved spectra along the stagnation streamline of the model, which is located 34.5 cm downstream of the nozzle exit for the forward position and 36.9 cm for the backward position. Each experiment recorded LOS radiation at eight spatial locations along the stagnation streamline of the model; and moving the model to the so-called forward and backward positions enabled complete coverage of the shock layer. The experimental setup and data are described in detail by Park et al.[4] The measured spectra contain molecular band systems of N_2, NO, N_2^+, CN, and atomic lines of N and O. Also, during the facility operation, both pressure and stagnation point heating measurements are made using a 4-in. diam water-cooled hemisphere.

Computational Approach

The building blocks of the present computational analysis are 1) simulation of nonequilibrium flow in the converging-–diverging conical nozzle and supersonic jet, 2) simulation of nonequilibrium shock-layer flow over the flat-faced cylinder model, and 3) prediction of LOS radiation from the computed flowfield.

An axisymmetric formulation is employed for computations of nonequilibrium flows in the arcjet facility. The present air model has 12 chemical species (N_2, O_2, NO, N, O, N_2^+, O_2^+, NO^+, N^+, O^+, e^-, and Ar), and the thermal state of the gas is described by three temperatures (T, T_r, and T_v): translational, rotational, and vibrational (vibrational–electronic), respectively. The governing Navier–Stokes equations are supplemented with equations accounting for thermochemical nonequilibrium processes and solved numerically using an implicit, finite volume method.

For computations of the expanding nozzle flow and supersonic jet, the nonequilibrium nozzle code of Ref. 6 is employed (updated to the 12-species model). The thermochemistry model—reaction set and rate coefficients—as described by Ref. 6, is a two-temperature version of the multitemperature model by Park and Lee.[7]

For computations of the shock-layer flow, the nonequilibrium blunt-body code of Refs. 8 and 9 is used. The two-temperature model of Park[10] is employed for the reactions and rate coefficients. More information on the thermochemical model and computational code can be found in Refs. 8 and 9. The reaction rates used for expanding flows and shock layers are different: the most important difference is in the reaction rates for NO exchange reactions.[7]

For computations of LOS radiation, a nonequilibrium radiation code (NEQAIR)[11] is used to predict emission spectra from the computed flowfield. The spectroscopic database for the NEQAIR code includes the recent improvements by Laux.[12] For all computations in this work, the nonequilibrium quasi-steady-state portion of NEQAIR is not used, and excited

states are assumed to be populated according to the Boltzmann distribution with translational, rotational, and vibrational temperatures. The vibrational temperature is used for electronic temperature.

For comparisons of computations with the experimentally determined flow properties, a LOS-averaging procedure is described in the next section.

LOS-Averaged Properties

The flow properties deduced from the experimental spectra, such as vibrational and rotational temperatures, represent LOS intensity-averaged values. To make a strict comparison between the experimentally determined flow properties and computations, a similar averaging needs to be carried on the computed flow properties. The averaging rule is set by the solution of radiative transfer equation along the LOS and the method by which average flow properties are extracted from the measured spectra.

The measured spectral intensity represents an integration of radiation along a particular LOS. For emission-dominated flows, i.e., optically thin gas, solution of the equation of radiative transfer for the intensity at wavelength λ is given by

$$I_\lambda(s) = I_\lambda(0) + \int_0^s E_\lambda \, ds \qquad (1)$$

where E_λ is the radiative emission. For a LOS consisting of n slabs with thickness Δs_i and no boundary contribution

$$I_\lambda(s_0) = \int_0^{s_0} E_\lambda \, ds = E_\lambda^0 s_0 = \sum_{i=1}^{n} E_\lambda^i \Delta s_i \qquad (2)$$

where E_λ^0 and s_0 are defined as the LOS-averaged emission at wavelength λ and total slab thickness, respectively.

Generally, the temperature information of various species is deduced from the ratios of intensities integrated over wavelength, i.e.,

$$R = A_1/A_2 = \int_{\lambda_1}^{\lambda_1 + \Delta\lambda_1} I_\lambda \, d\lambda \Big/ \int_{\lambda_2}^{\lambda_2 + \Delta\lambda_2} I_\lambda \, d\lambda \qquad (3)$$

where A_1 and A_2 represent integrated intensities. An appropriate choice of λ_1 and λ_2 provides a necessary sensitivity for the particular temperature determination (vibrational, rotational, or electronic). Figure 2 shows the wavelengths and areas (integrated emission) that are used to determine rotational and vibrational temperatures of N_2^+.[4] Note that the baseline of the areas is offset from absolute zero to reduce the effect of unresolved background radiation.
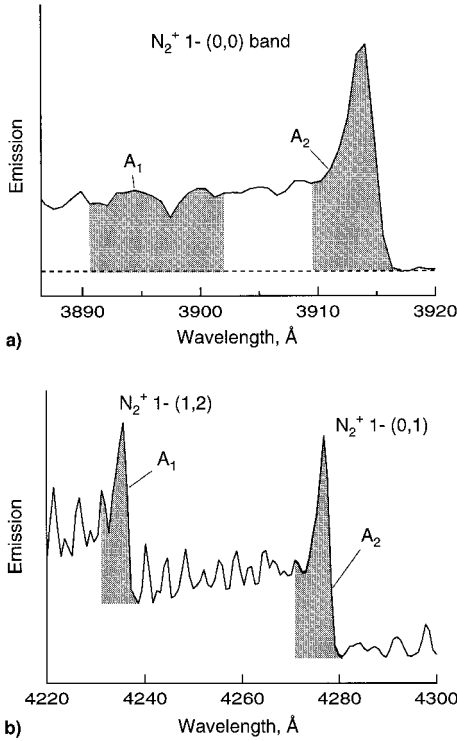
Fig. 2 Wavelengths and areas of integrated emission for determination of a) rotational and b) vibrational temperatures from N_2^+ spectra.

For emission-dominated flows, Eq. (3) can be put in the form

$$A_1/A_2 = \frac{E_1^0}{E_2^0} = \frac{\sum E_1^i \Delta s_i}{\sum E_2^i \Delta s_i} \quad (4)$$

which provides the averaging rule for temperatures along the LOS.

The integrated emission E generally depends on the temperatures and number density of radiating species. For a two-temperature gas, the emission can be assumed to have the functional form $E = CN_t f(T_v)g(T_r)$, where C is a constant and N_t is total number density of radiating species.

To determine the LOS-averaged rotational and vibrational temperatures, T_r^0 and T_v^0, two equations are then constructed using Eq. (4). For rotational temperature

$$\frac{f_{1r}(T_v^0)g_{1r}(T_r^0)}{f_{2r}(T_v^0)g_{2r}(T_r^0)} = \frac{\sum N_t^i f_{1r}(T_v^i)g_{1r}(T_r^i)\Delta s_i}{\sum N_t^i f_{2r}(T_v^i)g_{2r}(T_r^i)\Delta s_i} \quad (5)$$

and for vibrational temperature

$$\frac{f_{1v}(T_v^0)g_{1v}(T_r^0)}{f_{2v}(T_v^0)g_{2v}(T_r^0)} = \frac{\sum N_t^i f_{1v}(T_v^i)g_{1v}(T_r^i)\Delta s_i}{\sum N_t^i f_{2v}(T_v^i)g_{2v}(T_r^i)\Delta s_i} \quad (6)$$

Eqs. (5) and (6) need to be solved simultaneously for T_r^0 and T_v^0. For functions $f(T_v)$ and $g(T_r)$, curve-fits are generated from the NEQAIR computations of integrated emission obtained at a wide range of rotational and vibrational temperatures, and these are given in the Appendix. From the curve-fits, it is seen that the vibrational temperature T_v^0 dependence in Eq. (5) is weak. Using this fact, a reasonable solution methodology is as follows: First, assuming $f_{1r}/f_{2r} = 1$, Eq. (5) is solved for T_r^0 using the Newton–Raphson method; then Eq. (6) is solved for T_v^0; and this process is repeated with the updated temperatures. This iteration converges within four steps.

Similarly, to compare the computations with the experimental LOS-averaged total number density of N_2^+, the computed integrated number density is obtained from A_1 of Fig. 2b, i.e.,

$$A_1 = E_1^0 s_0 = \sum E_1^i \Delta s_i$$

or

$$N_t^0 s_0 = \frac{\sum N_t^i f_{1v}(T_v^i)g_{1v}(T_r^i)\Delta s_i}{f_{1v}(T_v^0)g_{1v}(T_r^0)} \quad (7)$$

where N_t^0 is the LOS-averaged number density, and s_0 is the shock-layer thickness.

It should be noted that the preceding LOS-averaging procedure to obtain T_r^0, T_v^0, and N_t^0 is consistent with the experimental determination of the LOS-averaged properties. In other words, for a given LOS-flowfield profile, if the synthetic spectra were generated using NEQAIR, and the LOS-averaged properties were deduced from this spectra using the methodology described by Park et al.,[4] these values would then be identical to T_r^0, T_v^0, and N_t^0.

Presentation of Results

The results will be covered in three subsections: 1) flowfield simulation in which computational simulations of the arcjet nozzle flow and shock layer flow are described, 2) comparison of average flow properties in which computed and experimentally obtained flow properties are compared, and 3) comparisons of radiation spectra in which direct comparisons of experimental and computed spectra are presented.

Flowfield Simulation

One of the difficulties in the simulation of an arcjet experiment is that an important parameter of the test, total flow enthalpy, is not known accurately. Using the stagnation point heating and pressure measurements from a hemisphere calorimeter and a Fay–Riddell type correlation,[13] total enthalpy of the flow is estimated to be 18.5 MJ/kg. Three sets of computations are carried out within approximately ±10% of the estimated enthalpy; for each case, the equilibrium temperatures behind the shock wave differ by 120 K. The set of computations presented here corresponds to the reservoir conditions of $p_0 = 6.8$ atm, $h_0 = 20.41$ MJ/kg, with the AHF 12-in. nozzle configuration. The nozzle computations are carried out using 100×50 grid points (50 normal to the wall). The flow at the nozzle entrance is assumed to have uniform temperature and velocity profiles and equilibrium composition. Figure 3 shows the AHF 12-in. nozzle geometry and the computed flowfield contours of translational–rotational and vibrational temperatures. The computations predict that the flow is chemically and vibrationally frozen before it reaches the nozzle exit. The vibrationally frozen flow can be easily observed in diverging section of the nozzle (Fig. 3b).

It is known from the facility test-box pressure measurements and/or visual observations that the flow after the nozzle exit continues to expand in a supersonic jet. However, because the extent of this expansion is not known accurately, the flow is simply expanded at a constant angle until the measured model surface pressure is duplicated to determine the freestream conditions for the shock-layer flow computations. The following is a summarization of the computed arcjet freestream conditions for the shock-layer flow. $h_0 = 20.41$, MJ/kg; $p_s = 83$ torr; $u_\infty = 5008$ m/s; $p_\infty = 200.3$ Pa; $\rho_\infty = 4.739 \times 10^{-4}$ kg/m³; $T_\infty = 1151$ K; $T_{r\infty} = 1162$ K; $T_{v\infty} = 2902$ K; $c_{N_2\infty} = 0.6443$; $c_{O_2\infty} = 0.1645 \times 10^{-4}$; $c_{NO\infty} = 0.3143 \times 10^{-5}$; $c_{N\infty} = 0.8431 \times 10^{-1}$; $c_{O\infty} = 0.2214$; $c_{N_2^+\infty} = \le 0.1 \times 10^{-9}$; $c_{O_2^+\infty} = 0.3818 \times 10^{-8}$; $c_{NO^+\infty} = 0.7405 \times 10^{-9}$; $c_{N^+\infty} = 0.9314 \times 10^{-7}$; $c_{O^+\infty} = 0.7680 \times 10^{-7}$; $c_{e\infty} = \le 0.1 \times 10^{-9}$; and $c_{Ar\infty} = 0.5000 \times 10^{-1}$. Although the freestream rotational temperature was measured
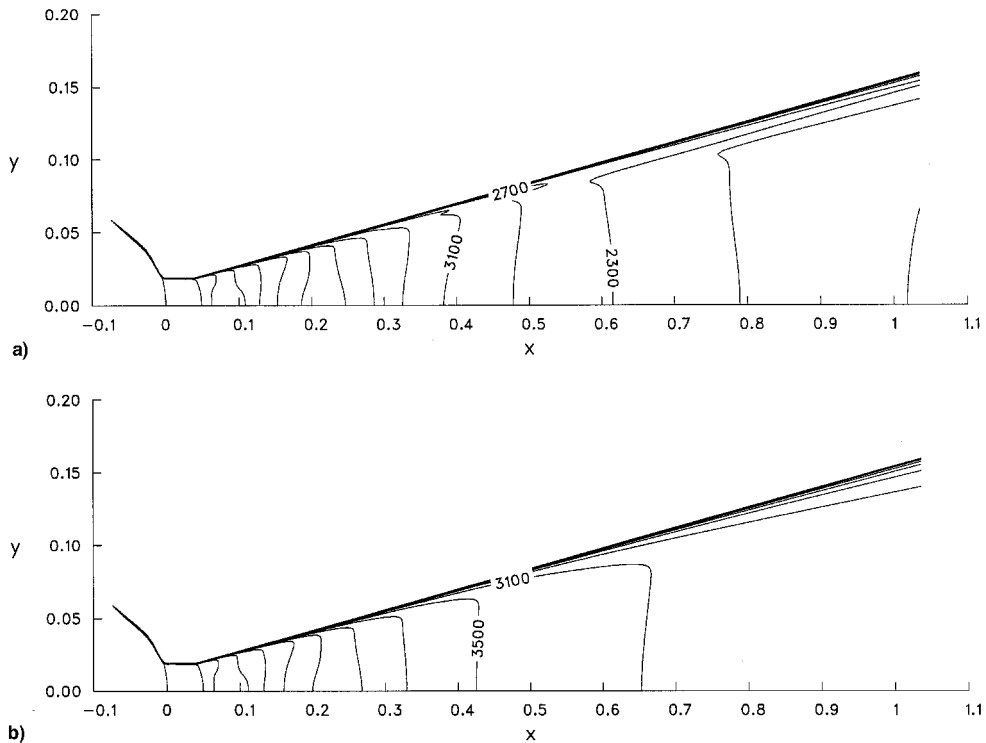
Fig. 3 Computed flowfield contours of AHF 12-in. nozzle (dimensions are in meters): p_0 = 6.8 atm, h_0 = 20.41 MJ/kg, air with 5% argon: a) translational–rotational temperature ($T = T_r$, DT = 400 K) and b) vibrational temperature (DT_v = 400 K).

from NO spectra (T_r = 900 ± 70 K),[4] at this point no effort was made to reproduce it in the computations mostly caused by the uncertainties where NO emission comes from in the arcjet freestream along the LOS direction.

Computations for the shock-layer flow over a 6-in.-diam, flat-faced cylinder model are performed using 60 × 80 grid points (80 normal to the wall). In computations, adaptive grid near the shock wave and boundary layer is also implemented. Figure 4 shows the computed flowfield contours of temperatures over the model. Examination of the flowfield shows that a significant portion of shock-layer flow is predicted to be in thermal equilibrium. From the contour plots, the shock layer has a relatively uniform core region with variations near the shock wave (direction normal to freestream flow). The uniformity along the LOS is a desirable feature if LOS-averaged temperature measurements are made to characterize the flow enthalpy. Also, because the experimental data only contain integrated LOS information, variation of the flow properties along the LOS is important to interpret the data.

Figure 5 shows the variation of the computed temperatures and N_2^+ number density along the LOS paths at the measurement locations between 9.0 and 20.7 mm upstream of the model. Here, the distance along the LOS represents the distance from the spectrometer (normal to the flow direction). As seen from Fig. 5a, the translational and rotational temperatures are equilibrated. In fact, for the present flow condition, this is valid throughout the flowfield. Note that the translational––rotational temperature and N_2^+ number density show significant variations along the LOS with respect to their values at the shock-layer core. Because of such nonuniformity, the LOS-averaged rotational temperatures obtained using Eqs. (5) and (6) are larger than the core rotational temperatures. On the other hand, the vibrational temperatures along the LOS seen in Fig. 5a show nearly step-function-like behavior, and therefore the LOS-averaged vibrational temperatures are very similar to the core vibrational temperatures.

The flow properties at the shock-layer core are well characterized by the flow properties at the stagnation streamline. Figure 6 shows the computed profiles of temperatures and spe-

cies mass fractions along the stagnation streamline where the distance from the model surface is normalized by the radius (R = 7.62 cm). Again, the thermal equilibrium region behind the shock is clearly observed. To examine the extent of chemical nonequilibrium behind the shock, a one-dimensional shock-wave flow is calculated with the freestream conditions. The computed equilibrium values behind the shock wave (T_{eq} = 6039 K, c_{Neq} = 0.2741, $c_{N_2^+eq}$ = 0.2490 × 10^{-5}) are also shown in Fig. 6. It appears that although a substantial portion of the shock-layer flow is in thermal equilibrium, near-chemical equilibrium conditions only exist at the axial locations close to the model. Note that the computed dissociation level and temperatures are closer to the equilibrium values than the computed N_2^+ mass fraction. As seen from Fig. 6b, the N_2^+ mass fraction shows a large variation along the stagnation streamline similar to the profiles in Fig. 5b. This variation in the N_2^+ number density is important because most of the averaged flow properties are deduced from the experimental spectra of the N_2^+ $1-$ system.

Comparison of Average Flow Properties

Analysis of the experimental data produced various LOS-averaged flow properties at several axial locations within the shock layer of the 6-in. model.[4] In this section, the computed results are compared with those deduced from the experimental spectra.
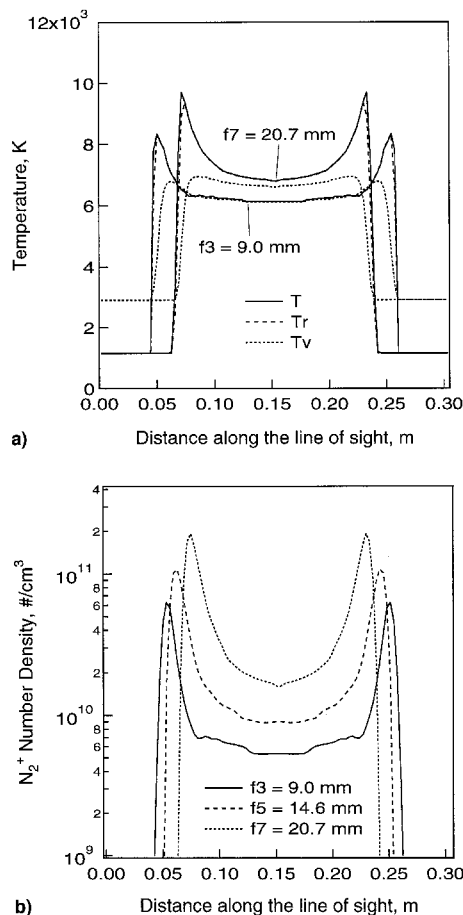
Figure 7 shows the comparison of LOS-averaged rotational and vibrational temperatures at several axial locations along the stagnation streamline. The computed LOS temperatures are determined using Eqs. (5) and (6). Because the measurements cover the entire shock layer, the shock standoff distance is observed to be 34.5 ± 1.5 mm. Computations predict the shock standoff distance within the same accuracy. The experimental data show that the rotational temperatures are higher than the vibrational temperatures throughout most of the shock layer. Despite the relatively large uncertainty bars in the experimental temperatures, a relaxation process behind the shock is discerned. The computed rotational temperatures are also consistently higher than vibrational temperatures and these

a)

b)
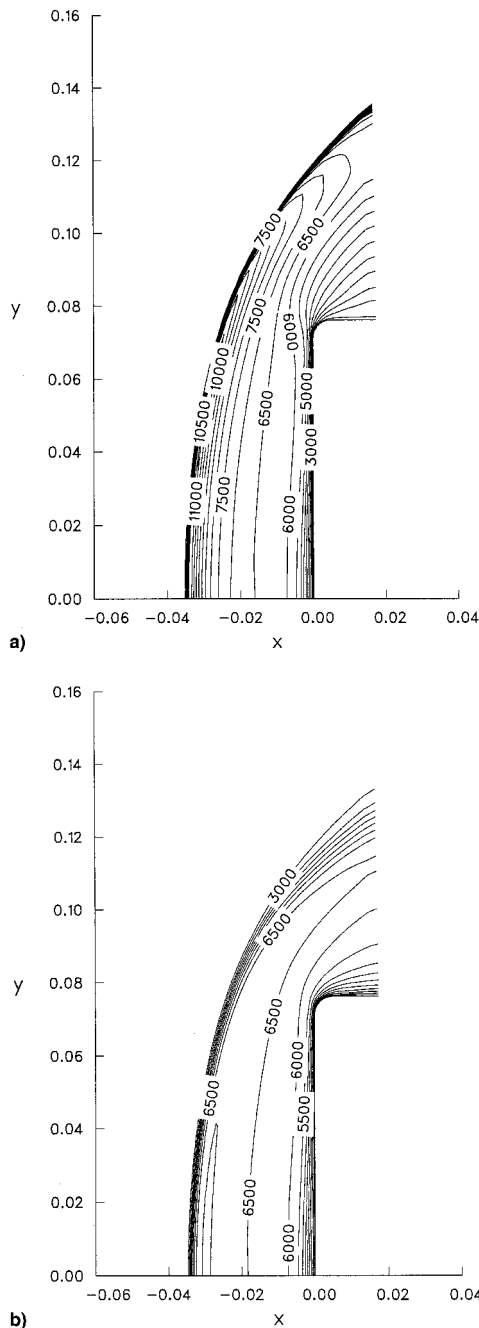
Fig. 4   Computed flowfield contours of arcjet shock layer over the 6-in. model (dimensions are in meters): a) translational temperature (DT = 500 K) and b) vibrational temperature (DT_v = 500 K).

a)

b)

Fig. 5   Variation of computed flow properties along the LOS paths: a) temperatures and b) N$_2^+$ number density.

also indicate a relaxation process. As mentioned before, even though thermal equilibrium exists at the core of shock layer, because of variations along the LOS, the computed-averaged rotational temperatures are higher than the core temperature. Therefore, the observed higher rotational temperatures from the spectra do not necessarily indicate a thermal nonequilibrium at the core of shock layer.

Figure 8 shows the comparison of computed and experimental N$_2^+$ number density at several axial locations along the stagnation streamline. The shock-layer thickness s_0, over which the flow properties are integrated, is also plotted. The experimental values deduced from the LOS-spectra, i.e., from the intensity of N$_2^+$ 1− (1, 2) band (Fig. 2b), represent the number density integrated over the shock-layer thickness. In this integration, the number density is not equally weighted along

the LOS, therefore it is different from the actual total number density of N$_2^+$ in the shock layer. Accordingly, the computed values also represent the LOS-averaged quantities, which are obtained using Eq. (7). From Fig. 8, the computations appear to overestimate the N$_2^+$ number density at spatial locations near the shock and underestimate them at locations near the model. Near the shock front, the averaging process is suspect because the LOS includes a mostly nonequilibrium shock region and the shock-layer thickness is varying significantly. However, as one approaches the model, the computed N$_2^+$ number density appears to be decreasing at a faster rate than the experimental values indicate. This may be attributable to dissociative recombination rates of N$_2^+$. Also, because of the present optical system in the experiment, the spatial resolution near the shock is such that the measured intensity tends to be smoothed out along the axial locations.[4]

Comparison of Radiation Spectra

As mentioned earlier, the experimental data include the LOS intensity measurements for several wavelength regions and at several axial locations along the stagnation streamline. In this section, direct comparisons of the computed intensities with the experimental data are presented. It should be noted that the LOS intensity is generally a function of temperatures and the excited number density of radiating species. The excited number density is linearly proportional to the species density and functionally dependent on temperatures, which varies significantly from one radiating system to another. As a sensitivity guideline for the following comparisons of spectra, at a temperature of 6000 K, if the temperature (electronic) were increased by 200 K the emission intensity from N$_2$ 2+, O, and N atom lines would nearly double, and the emission intensity from N$_2^+$ 1− and NO γ would increase by approximately 20
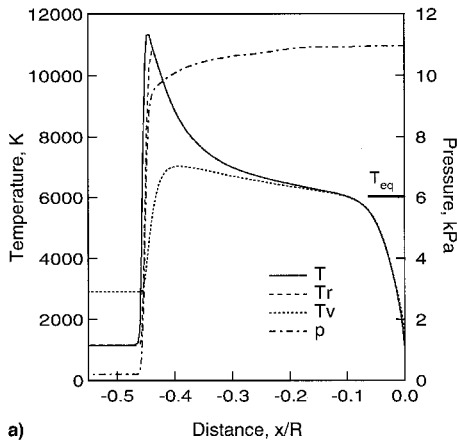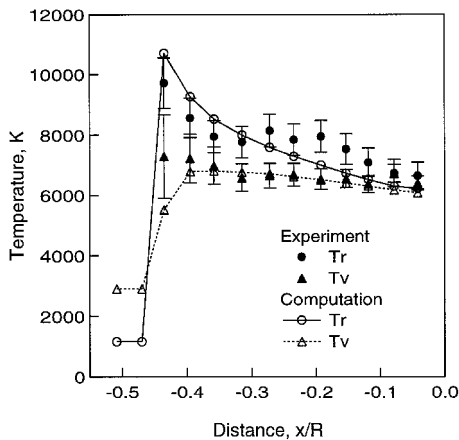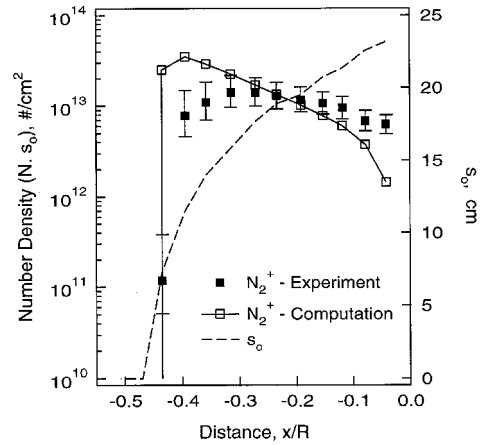
a)
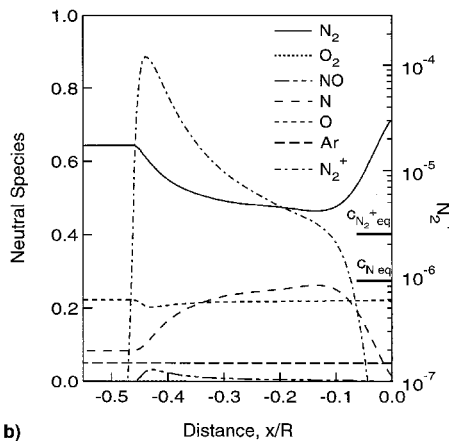
b)

Fig. 6 Computed flow properties along the stagnation streamline of the 6-in. model: a) temperature and pressure and b) neutral species and vibrational temperatures.

Fig. 7 Comparison of LOS-averaged rotational and vibrational temperatures.

Fig. 8 Comparison of LOS-integrated N_2^+ number density.

and 40%, respectively. Also, note that the measured intensity values are certain within $\pm7\%$ wavelengths above 2500 Å and $\pm16\%$ wavelengths below 2500 Å,[4] and that there is a wavelength difference of 0.7–1.2 Å between the measured and computed spectra because of the present wavelength calibration and resolution of the experimental data.

Comparisons of spectra in the wavelength range of 4000–4400 Å at several axial locations along the stagnation streamline are presented in Figs. 9 and 10. The spectra shown are composed of emission from three molecular systems: 1) CN violet, 2) N_2 2+, and 3) N_2^+ 1−. The dominant band structure starting at 4280 Å is that of the N_2^+ 1− system. Both the CN

violet and N_2 2+ emission are weaker than the N_2^+ 1− emission, and they occur at the shorter wavelength side of Figs. 9 and 10. The two strongest peaks in the N_2^+ emission are the (0, 1) and (1, 2) bandheads, and they occur at wavelengths where the CN violet and N_2 2+ emission is becoming negligible. For this reason, they are useful indicators of average temperatures and integrated number density for N_2^+ in the shock-layer flow. The signals from these two bandheads are used to determine vibrational temperature and N_2^+ number density as a function of distance along the stagnation streamline, which were compared with computations in Figs. 7 and 8.

Observing Figs. 9 and 10 from the flow direction, the experimental emission spectra are seen to increase in value from a relatively low level to a maximum at the spatial location f8. In addition, the spectral features between the stronger peaks also show increasing intensity going toward the f8 location. These qualitative attributes are derived from the increasing integrated population of N_2^+ and/or the increasing temperature. From the location f8 on toward the model, the decreasing intensity is probably caused by a decreasing N_2^+ population, and to a lesser degree by decreasing vibrational temperature.

The computed emission spectra arise from a zero level in the freestream, reach a maximum at the spatial location b2, and then decrease toward the model. In comparison, the rate of increase and decrease in the computed spectra appear to be faster than that of the experiment; similar to the observations made for Fig. 8. Also note that the computed N_2^+ number density has large variations in the shock layer as shown in Figs. 5b and 6b. For the middle spatial locations, b1 through f6, the overall agreement is fairly good between the computed and measured emission spectra. By the last three positions near the model, f1–f3, the computed intensity level is substantially less than the measured intensity. It should be noted that the LOS f1 goes through the boundary layer of the computed flowfield. This discrepancy in N_2^+ radiation is the cause of differences in number densities presented in Fig. 8. The disagreement at the last spatial locations is most apparent in the region below 4210 Å, where the CN violet and N_2 2+ contributions are greater. Because CN was not included as a species in the flow model, this may partially explain the underprediction of the signal.

In Figs. 11–17, the computed LOS spectra are compared with the experimental spectra at the spatial location f7 = 20.7 mm upstream of the model. These comparisons cover most of the wavelength region that was experimentally investigated. A detailed analysis of these spectra is outside the scope of this paper. Therefore, a brief explanation for each spectrum will be given. More detailed information on identification of spectra can be found in Park et al.[4]

Figure 11 shows the emission spectrum for the wavelength range of 2000–2800 Å. At these wavelengths the dominant emitter is NO, which has a number of closely spaced excited
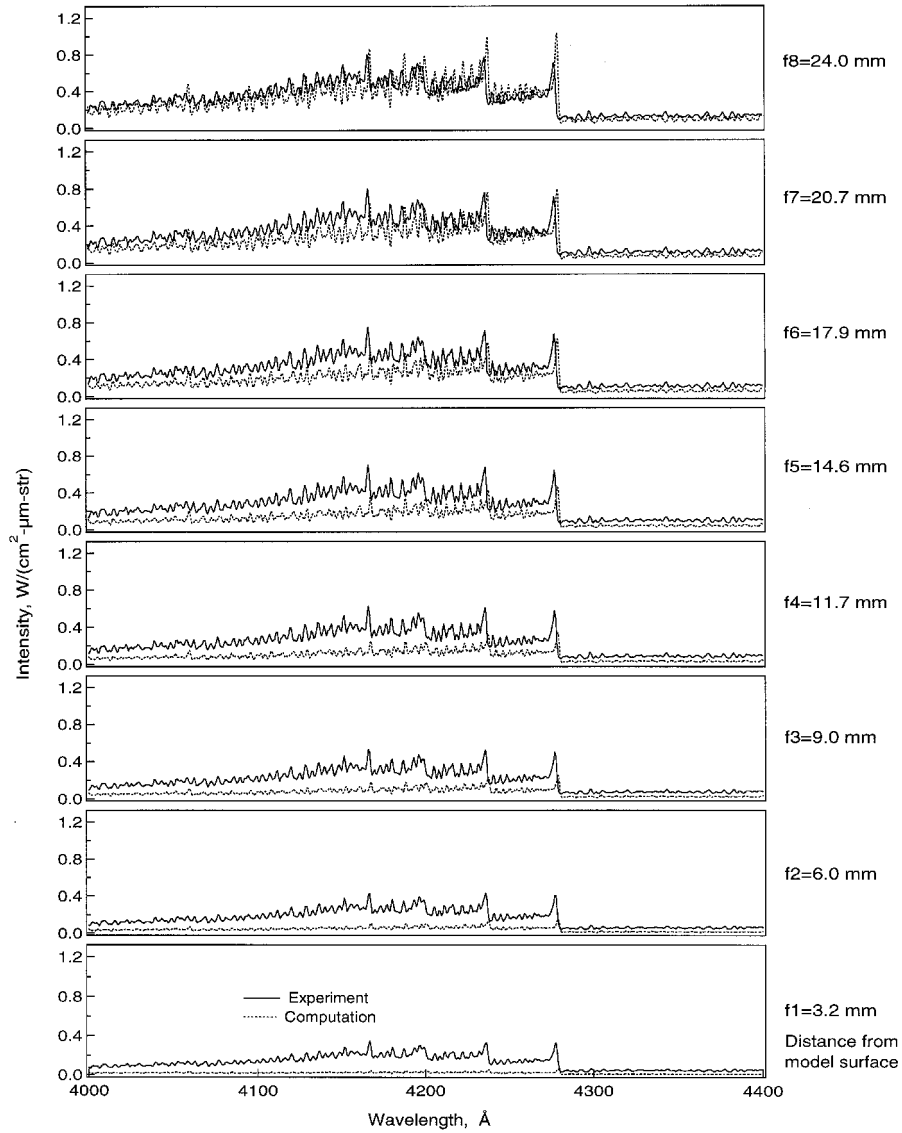
Fig. 9 Comparison of computed and experimental spectra at the forward model position locations.
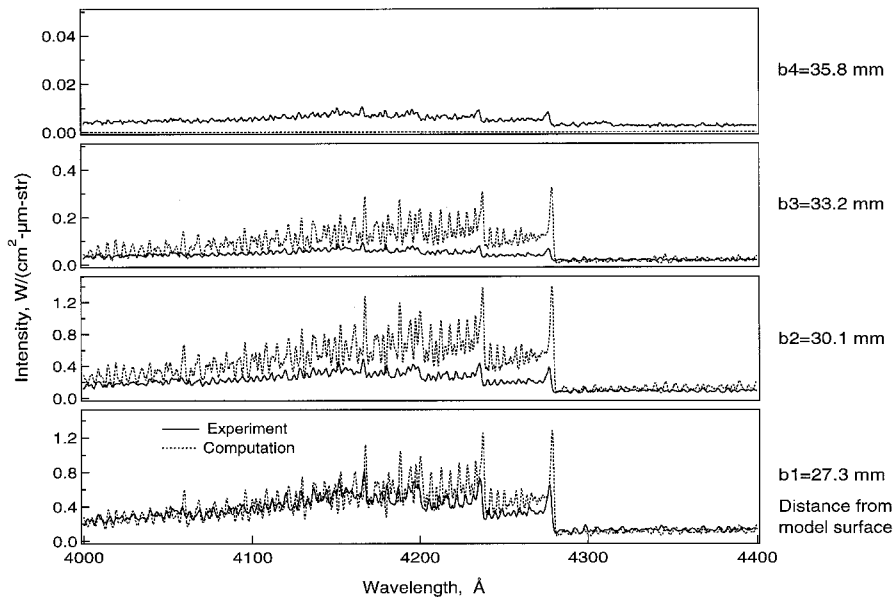

Fig. 10 Comparison of computed and experimental spectra at the backward model position locations.
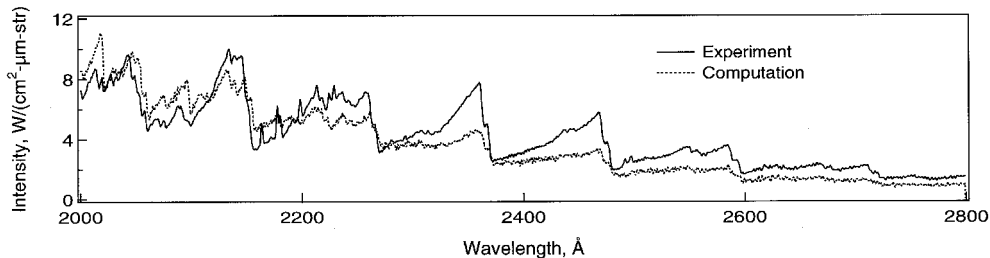
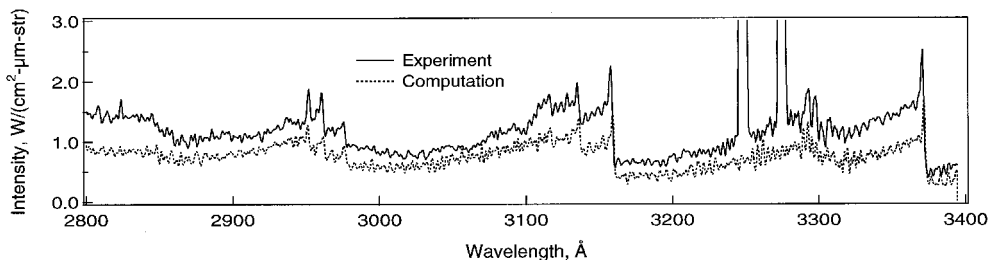**Fig. 11   Comparison of computed and experimental spectra at f7: NO molecular bands.**

Fig. 12   Comparison of computed and experimental spectra at f7: N_2^+ and N_2 molecular bands.
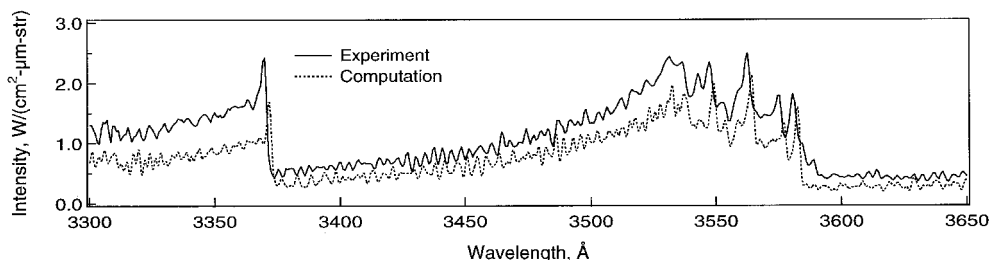

Fig. 13   Comparison of computed and experimental spectra at f7: N_2^+ and N_2 molecular bands.
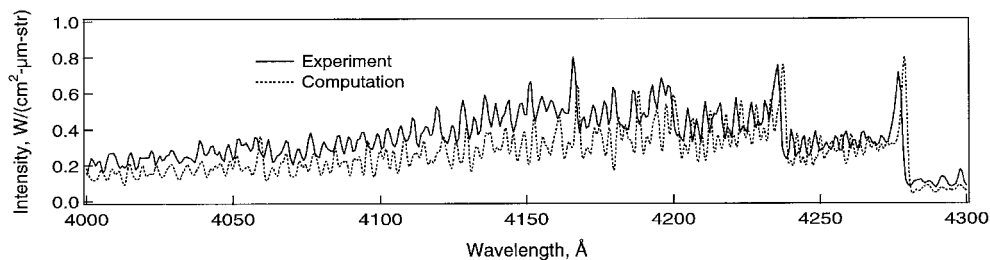

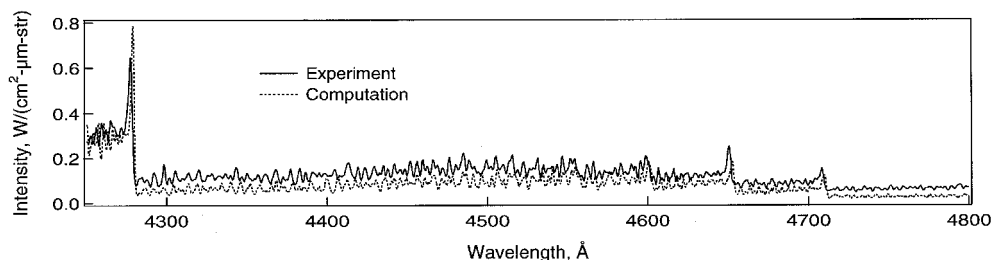**Fig. 14   Comparison of computed and experimental spectra at f7: N_2^+ molecular bands.**

Fig. 15   Comparison of computed and experimental spectra at f7: N_2^+ molecular bands.

electronic states. Consequently, the spectrum is composed of overlapping emission from the NO γ, NO β, NO δ, and NO ε systems, which makes it difficult to extract temperature information from the spectra. Most of the dominant peaks are NO γ features, which are explicitly identified by Park et al.[4] The computed spectrum appears to match the measured emission fairly well at the shorter wavelengths but appears to underpredict the emission at longer wavelengths, which is most

noticeable at the peaks near 2400 Å. Computations, not shown here, indicate that most of the NO radiation may come from the nonequilibrium shock front, and nonuniformity in NO number density along the LOS is significant.

Figure 12 covers the emission spectrum for the wavelength range of 2800–3400 Å. The two off-scale features in the experimental spectrum are Cu atom lines; copper is present in the flow as a contaminant from erosion of electrode surfaces
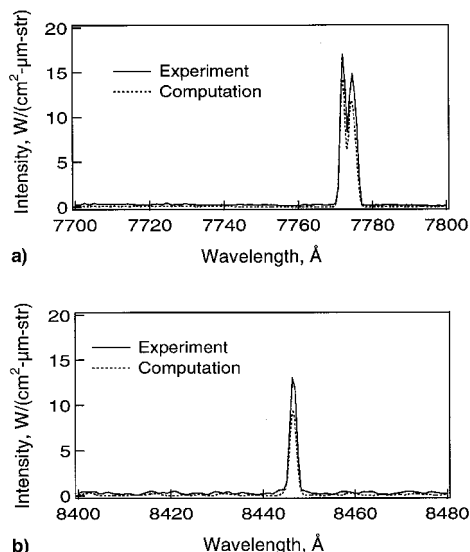
Fig. 16 Comparison of computed and experimental spectra at f7: atomic lines of O: a) O ($3P$ $^5S^0$ 2 $3P$ ^5P) and b) O ($3P$ $^3S^0$ 2 $3P$ ^3P).
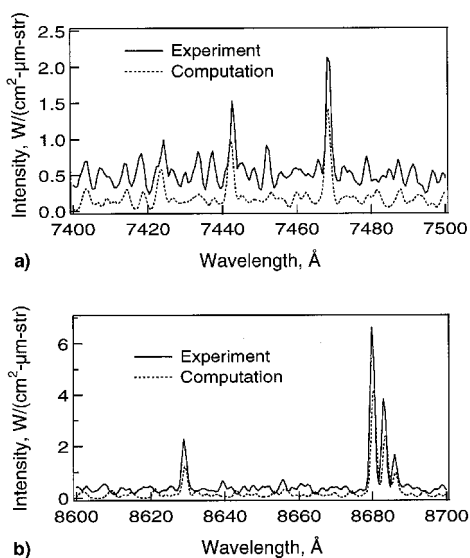

Fig. 17 Comparison of computed and experimental spectra at f7: atomic lines of N: a) N ($3P$ ^4P 2 $3P$ ^4S) and b) N ($3P$ ^4P 2 $3P$ $^4P^0$).

in the constricted arc heater. The remaining spectrum is from the molecular systems: N_2 2+, N_2^+ 1−, and NO. N_2 2+ is the strongest emitter in the region, and the two most prominent peaks are the (0, 0) and (1, 0) band heads at 3371 and 3159 Å, respectively. Overall, the agreement between the computed and measured emission spectra is fairly good. The relative strengths of the calculated (1, 0) and (0, 0) bandheads appear to match the measured values. Note that emission from N_2 2+ in this wavelength range is very sensitive to temperature variations. It is possible that the computed N_2 number density and/or vibrational temperature may be lower than the experiment at this spatial location. If the computed spectrum were shifted upward by a constant value, the agreement would improve. This may indicate that some background radiation, which is not included in the modeling, is present in the experiment.

Computed and measured emission spectra for the wavelength range of 3300–3650 Å are presented in Fig. 13. In this wavelength region, the primary emitters are again molecular systems: N_2 2+, N_2^+ 1−, and CN violet. The prominent peak

at 3371 Å is the (0, 0) bandhead of N_2 2+, and the multipeak feature near 3550 Å contains several bandheads of N_2^+ 1− as well as the (0, 1) bandhead of N_2 2+ and the (1, 0) bandhead of CN violet. Owing to the species overlap in this spectral feature, it is difficult to obtain quantitative information from any individual bandhead. However, the comparison does appear to indicate that prediction of the N_2^+ number density is closer than prediction of the N_2 number density. The relative peak heights of the bandheads appear to be fairly well predicted, and this may again indicate that the temperatures used in the computation match the flow temperatures well.

Figures 14 and 15 show computed and measured emission spectra over the 4000–4300 and 4300–4800 Å spectral regions. For these regions, N_2^+ is the dominant emitting species, with some minor N_2 2+ and CN violet system emission at the shorter wavelengths. The comparison is quite favorable between the computed and measured spectra. Relative strengths of the spectral peaks are fairly well matched, and the overall signal levels are close, indicating that both average temperature and total number density along the LOS at this location are well simulated. The rotational structure, which comprises the smaller peaks in between the larger bandheads in Fig. 14 also appears to be adequately simulated.

Finally, the measured and predicted infrared emission spectra from atomic lines of N and O are presented in Figs. 16 and 17. At these wavelengths, in addition to a possible stray light background signal, there is some underlying molecular emission, mainly from the N_2 1+ system. The atom emission lines are predicted within 20–35%, and this is considered to be good agreement considering the previously mentioned temperature sensitivity of the intensity.

Summary and Concluding Remarks

Computational simulations of the shock-layer emission experiments at the NASA Ames Research Center's arcjet tunnel are presented. The experimental data include spatially resolved emission spectra of radiation emanating from a shock layer formed in front of a flat-faced cylinder model. Multitemperature nonequilibrium codes are used to compute the flowfield, and a LOS radiation code is employed to predict the spectra from the computed flowfield.

For this experimental condition, computations indicate that the shock-layer core is mostly in thermal equilibrium and near-chemical equilibrium only at the spatial locations close to the model. Computations also predict that the rotational temperature and N_2^+ number density variations along the LOS are significant. These variations must be taken into account in interpretation of the flow properties deduced from the shock-layer emission spectra.

The computed LOS-averaged rotational and vibrational temperatures are in reasonably good agreement with those deduced from the experimental spectra. There are differences between the computed and experimental LOS-averaged number densities of N_2^+. The computed LOS intensities are directly compared with the measurements at several locations in the shock layer. The compared spectra include molecular band systems of N_2, NO, N_2^+, and atomic lines of N and O, and overall computations show reasonably good agreement with the experiment.

The temperature and number density measurements so far are not sufficient for assessment of thermochemical equilibration processes in the arcjet shock layer. It should be noted that if the uncertainties in temperature and number density measurements are significantly reduced and the complete assessment of thermochemical equilibration processes is made (LOS distributions of flow properties are resolved experimentally), then it may be feasible to deduce the total flow enthalpy from emission measurements.

Appendix: LOS-Averaging Functions

The curve-fits for functions $f_r(T_v)$ and $g_r(T_r)$

$$\ell n\, f_{1r}(T_v) = 4.2029 - 0.71124 z_v - 8.9475 \times 10^{-1} z_v^2$$
$$+ 1.0029 \times 10^{-1} z_v^3$$

$$\ell n\, f_{2r}(T_v) = 4.2644 - 0.81416 z_v - 8.3995 \times 10^{-1} z_v^2$$
$$+ 9.1059 \times 10^{-2} z_v^3$$

$$g_{1r}(T_r) = 1.0282 \times 10^{-2} + 0.15202 z_r - 4.7673 \times 10^{-2} z_r^2$$
$$+ 7.4414 \times 10^{-3} z_r^3 - 4.6392 \times 10^{-4} z_r^4$$

$$g_{2r}(T_r) = 9.7883 \times 10^{-3} + 0.19254 z_r - 1.3929 \times 10^{-2} z_r^2$$
$$- 1.0679 \times 10^{-3} z_r^3 + 1.9201 \times 10^{-4} z_r^4$$

for functions $f_v(T_v)$ and $g_v(T_r)$

$$\ell n\, f_{1v}(T_v) = 5.0724 - 1.5397 z_v - 6.0161 \times 10^{-1} z_v^2$$
$$+ 5.2984 \times 10^{-2} z_v^3$$

$$\ell n\, f_{2v}(T_v) = 4.4855 - 1.2351 z_v - 6.0581 \times 10^{-1} z_v^2$$
$$+ 5.2204 \times 10^{-2} z_v^3$$

$$g_{1v}(T_r) = 1273.45 - 1245.78 \exp(-0.25850 z_r)$$

$$g_{2v}(T_r) = 2469.05 - 2463.27 \exp(-0.17904 z_r)$$

where $z_v = 10{,}000/T_v$ and $z_r = 10{,}000/T_r$.

Acknowledgments

References

[1]Scott, C. D., "Survey of Measurements of Flow Properties in Arcjets," *Journal of Thermophysics and Heat Transfer*, Vol. 7, No. 1, 1993, pp. 9–24.

[2]Sharma, S. P., Park, C. S., Newfield, M., Balboni, J., Scott, C. D., Arapelli, S., and Taunk, J., "Arcjet Flow Characterization," AIAA Paper 96-0612, Jan. 1996.

[3]Park, C. "Experimental Evaluation of Real-Gas Phenomena in High-Enthalpy Aerothermal Test Facilities," AIAA Paper 96-2207, June 1996.

[4]Park, C. S., Newfield, M., Fletcher, D. G., Gökçen, T., and Sharma, S. P., "Spectroscopic Emission Measurements Within the Blunt Body Shock Layer in an Arc-Jet Flow," AIAA Paper 97-0990, Jan. 1997.

[5]Peterson, A. B., Nichols, F., Mifsud, B., and Love, W., "Arc Jet Testing in NASA Ames Research Center Thermophysics Facilities," AIAA Paper 92-5041, Dec. 1992.

[6]Gökçen, T., "Computation of Nonequilibrium Viscous Flows in Arc-Jet Wind Tunnel Nozzles," AIAA Paper 94-0254, Jan. 1994.

[7]Park, C., and Lee, S. H., "Validation of Multitemperature Nozzle Flow Code," *Journal of Thermophysics and Heat Transfer*, Vol. 9, No. 1, 1995, pp. 9–16.

[8]Gökçen, T., "Effects of Freestream Nonequilibrium on Convective Heat Transfer to a Blunt Body," *Journal of Thermophysics and Heat Transfer*, Vol. 10, No. 2, 1996, pp. 234–241.

[9]Gökçen, T., "Effects of Flowfield Nonequilibrium on Convective Heat Transfer to a Blunt Body," *Journal of Thermophysics and Heat Transfer*, Vol. 11, No. 2, 1997, pp. 289–295.

[10]Park, C., "Review of Chemical-Kinetic Problems of Future NASA Missions, I: Earth Entries," *Journal of Thermophysics and Heat Transfer*, Vol. 7, No. 3, 1993, pp. 385–398.

[11]Park, C., "Nonequilibrium Air Radiation (NEQAIR) Program: User's Manual," NASA TM 86707, July 1985.

[12]Laux, C. O., "Optical Diagnostics and Radiative Emission of Air Plasmas," Stanford Univ., High Temperature Gas Lab., Rept. T-288, Stanford, CA, Aug. 1993.

[13]Pope, R. B., "Measurements of Enthalpy in Low-Density Arc-Heated Flows," *AIAA Journal*, Vol. 6, No. 1, 1968, pp. 103–110.